THE JOURNAL OF PHYSICAL CHEMISTRY C

Article

pubs.acs.org/JPCC

Aqueous-Phase Synthesis of Sub 10 nm $Pd_{core}@Pt_{shell}$ Nanocatalysts for Oxygen Reduction Reaction Using Amphiphilic Triblock Copolymers as the Reductant and Capping Agent

Geng Zhang,[†,‡] Zhi-Gang Shao,*[,†] Wangting Lu,[†,‡] Hui Xiao,[†,‡] Feng Xie,[†] Xiaoping Qin,[†] Jin Li,[†,‡] Fuqiang Liu,[§] and Baolian Yi[†]

[†]Fuel Cell System and Engineering Research Group, Dalian Institute of Chemical Physics, Chinese Academy of Sciences, 457 Zhongshan Road, Dalian 116023, People's Republic of China

[‡]Graduate School of Chinese Academy of Sciences, 19A Yuquan Road, Beijing 100049, People's Republic of China

[§]Electrochemical Energy Lab, Department of Material Science and Engineering, University of Texas at Arlington, Arlington, Texas 76019, United States

Supporting Information

ABSTRACT: Sub 10 nm $Pd_{core}@Pt_{shell}$ nanocrystals (NCs) were prepared by a facile and green reduction method in aqueous solutions using commercially available and nontoxic poly(ethylene oxide)−poly(propylene oxide)−poly(ethylene oxide) amphiphilic triblock copolymers as the reductant, stabilizer, and capping agent. The growth mode and morphology of the Pt shell on the Pd surface can be adjusted simply by the Pt/Pd molar ratio. The activity of carbon-supported Pd@Pt NCs toward oxygen reduction reaction exhibited a Pt shell morphology dependence, with $Pd_2@Pt_1$ (Pt/Pd molar ratio 1/2) having the highest mass activity and $Pd_1@Pt_2$ (Pt/Pd molar ratio 2/1) having the best area-specific activity, and both of them were significantly enhanced in comparison with that of commercial Pt/C catalysts. Moreover, single-fuel-cell testing indicated superior activity and durability of $Pd_2@Pt_1$ NCs, which made $Pd_2@Pt_1$ NCs promising cathode catalysts for fuel cell applications.

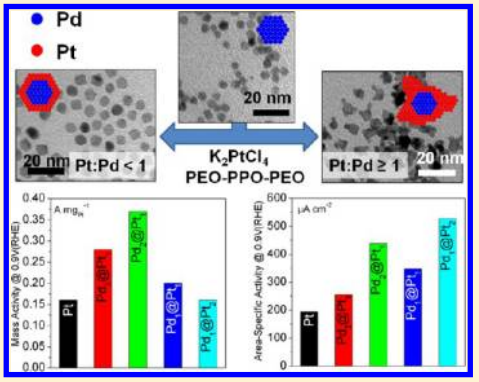

1. INTRODUCTION

In the past few years, binary noble metal nanocrystals (NCs) have received particular interest because of their catalytic properties, which are highly tunable and superior compared with those of their monometallic counterparts.[1−3] Besides the size and shape, the composition is another important factor that determines the catalytic properties of a binary noble metal NC.[1,4] PdPt NCs with a Pd core and Pt shell received considerable attention in the development of next-generation electrocatalysts for oxygen reduction reaction (ORR) in proton exchange membrane fuel cells (PEMFCs).[5−9] It is well-known that the PEMFC is considered to be a promising candidate for the future generation of power solutions for vehicles due to the high power density, high efficiency, and low emissions.[10] However, the commercialization of fuel cells has been impeded by the high cost and poor activity of commercial carbon black supported Pt catalysts for ORR.[11] $Pd_{core}@Pt_{shell}$-structured electrocatalysts were expected to be one of the most effective approaches to resolve these problems. In addition to the improved utilization of Pt atoms and lower price of Pd,[12] the ORR activity for a Pt monolayer on a Pd(111) surface was reported to surpass that of Pt(111) due to the geometric and electronic effects.[13,14]

The size, shape, and composition of binary noble metal NCs can be regulated in the synthesis process. Therein, the aqueous-phase system, acknowledged for its envrionmentally friendly, tunable, and technologically simple implementation, gets special attention.[2,3,15] However, the synthesis of bimetallic core−shell Pd@Pt NCs in aqueous solutions is still a challenge. Adzic's group prepared a series of Pt monolayer catalysts on Pd and other alloy cores using the electrochemical method,[9,16,17] but it suffers from complicated equipment and difficulty in large-scale synthesis.[18] Xia's group synthesized Pd@Pt NCs by means of seeded epitaxial growth.[19−21] Nevertheless, the obtained Pd@Pt NCs were usually larger than 10 nm, which is too large for ORR catalysts. In addition, poly(vinylpyrrolidone) (PVP) was used in their preparation. It is well-known that PVP interacts strongly with Pt, and it is very hard to remove PVP from the surface of Pt.[22] The remaining PVP will deteriorate the activity seriously.[23] Therefore, a facile aqueous-phase synthesis method for Pd@Pt NCs requires urgent development.

Furthermore, most reported aqueous-phase synthesis methods always involve the reduction of a metal salt by a reductant in the presence of a stabilizer; the reductant and stabilizer are generally two different reagents. However, the case

Received: February 7, 2013
Revised: May 19, 2013
Published: May 22, 2013

   dx.doi.org/10.1021/jp401375b | J. Phys. Chem. C 2013, 117, 13413−13423

with just one reagent as both the reductant and stabilizer simultaneously in preparation of binary noble metal NCs is still desirable and technically challenging, which has been tried in only limited studies to date.[24−26] Under such conditions, the preparation procedure will be simplified, accompanied by the potential appearance of NCs with distinct morphology and structure, owing to the specific reducing power for different metal precursors and the shape-controlling effect of that reagent.[27] Accordingly, it is a unique field under development and attracting increasing attention.

Herein, we utilized amphiphilic triblock poly(ethylene oxide)−poly(propylene oxide)−poly(ethylene oxide) [Pluronic F127 ($PEO_{106}PPO_{65}PEO_{106}$)] copolymers as the reductant to synthesize sub 10 nm binary Pd@Pt NCs with a core−shell structure. The PEO−PPO−PEO copolymers have been used as the structure-directing agent in the fabrication of a dendritic core−shell structure,[28−31] but the utilization of PEO−PPO−PEO as a reductant to prepare core−shell nanocrystals, to the best of our knowledge, has not been reported. Moreover, the F127 copolymers also acted as the stabilizer and capping agent during the deposition of Pt on a Pd surface. The growth mode of the Pt shell and the corresponding morphology could be controlled by the Pt/Pd molar ratio. Anyway, sub 10 nm Pd@Pt NCs could be successfully obtained by the method reported here. More importantly, the remaining F127 copolymers could be easily eliminated from the surface of NCs without complicated post-treatment as in the removal of poly(vinylpyrrolidone) (PVP).[32] As expected, Pd@Pt NCs exhibited outstanding activity toward ORR in comparison with the monometallic Pt NCs. Furthermore, Pd@Pt NCs presented excellent durability in single-fuel-cell testing, which is another important indicator for evaluating ORR catalysts. Additionally, this method is suitable for large-scale preparation due to the avoidance of electrochemical deposition. The product can be a promising candidate for commercial use in fuel cells, for the superior performance and significantly lowered Pt content.

2. EXPERIMENTAL SECTION

2.1. Material Synthesis. *2.1.1. Synthesis of Pd NCs.* First, 140 mg mL^{-1} Pluronic F127 (Sigma-Aldrich) aqueous solutions were prepared by dissolving F127 in deionized water in a round-bottom flask equipped with a reflux condenser and a Teflon-coated magnetic stirring bar. The flask was put into the oil bath at 80 °C. Then a given amount of 34.2 mM Na_2PdCl_4 (Aladdin, Shanghai, China) aqueous solution was injected into the above solution to give a final $PdCl_4^{2-}$ concentration of 4.2 mM. The reaction mixture was heated at 80 °C in air under vigorous stirring. After 2 h, Pd NCs were obtained.

2.1.2. Synthesis of Pd@Pt NCs. The as-prepared Pd NCs were used as the seeds for the preparation of Pd@Pt NCs. A given amount of 19.1 mM K_2PtCl_4 (Shenyang Research Institute of Nonferrous Metal, Shenyang, China) aqueous solution with a nominal Pt/Pd molar ratio of 1/3, 1/2, 2/3, 1/1, or 1/2 was injected into the above Pd colloid solution. After the resulting solution was stirred at 80 °C for 3 h, Pd@Pt NCs (denoted as $Pd_3@Pt_1$, $Pd_2@Pt_1$, $Pd_3@Pt_2$, $Pd_1@Pt_1$, and $Pd_1@Pt_2$ for the corresponding Pt/Pd molar ratio) were obtained.

2.1.3. Synthesis of Pt NCs. The preparation of Pt NCs was similar to that of Pd NCs. Briefly, 140 mg mL^{-1} Pluronic F127 aqueous solutions were prepared by dissolving F127 in deionized water in a round-bottom flask equipped with a reflux condenser and a Teflon-coated magnetic stirring bar. The flask was put into the oil bath at 80 °C. Then a given amount of 19.1 mM K_2PtCl_4 aqueous solution was injected into the above solution to give a final $PtCl_4^{2-}$ concentration of 3.8 mM. The reaction mixture was heated at 80 °C in air under vigorous stirring. After 3 h, Pt NCs were obtained.

2.1.4. Synthesis of Carbon-Supported Catalysts. For the preparation of supported catalysts, carbon blacks (Vulcan XC-72R) were uniformly dispersed in ethanol by sonication. The mass of carbon blacks used was 4 times that of Pd in the preparation of supported Pd and Pd@Pt catalysts (denoted as Pd/C and Pd@Pt/C); identically, carbon blacks with 4 times the Pt mass were added for supported Pt catalysts [denoted as Pt/C(F127)]. Then the carbon black suspension was added to the colloid solution of NCs followed by sonication for 30 min, and then the mixture was stirred overnight. The product was collected by centrifugation, followed by consecutive washing/centrifugation cycles with ethanol and water. The centrifugate was dried at 60 °C under vacuum overnight, and supported catalysts were obtained. The theoretical metal loading in the final catalysts was 20 wt % for Pd/C and Pt/C(F127) and 27, 33, 42, and 54 wt % for $Pd_3@Pt_1/C$, $Pd_2@Pt_1/C$, $Pd_1@Pt_1/C$, and $Pd_1@Pt_2/C$, respectively, but the true loading was evaluated by thermogravimetric analyses (TGA). Moreover, 50 wt % $Pd_2@Pt_1/C$ was prepared for fuel cell testing.

2.1.5. Membrane Electrode Assembly (MEA) Preparation. Catalyst-coated membrane (CCM) electrodes were used for single cell testing. The anode catalyst was 40 wt % Pt/C (Johnson Matthey, abbreviated as JM), while the cathode catalyst was $Pd_2@Pt_1/C$. The catalyst ink was prepared by ultrasonically blending electrocatalyst powder with Nafion solution (5 wt %, Du Pont Corp.) and 2-propanol for 30 min at an ionomer/carbon weight ratio of 0.7/1. The catalyst ink was then sprayed onto both sides of a Nafion 211 membrane on a hot plate at 60 °C. The true Pt loading was measured by inductively coupled plasma atomic emission spectroscopy (ICP-AES) and weighting. The MEA with a cathode metal loading of 0.15 mg_{Pd+Pt} cm^{-2} was prepared by 33%$Pd_2@Pt_1/C$, while MEAs with high cathode metal loadings (0.25 and 0.62 mg_{Pd+Pt} cm^{-2}) were fabricated using 50%$Pd_2@Pt_1/C$.

The MEAs with an active area of 5 cm^2 were fabricated by hot-pressing the wet-proofed carbon gas diffusion layer (GDL, Sunrise Power, China) on both sides of the CCM at 140 °C for 2 min. The MEA was then cooled and assembled in 5 cm^2 single cells for testing. For comparison, the state-of-the-art 50 wt % Pt/C(JM) was also used to prepare the cathode catalyst layer followed by the above-mentioned procedure.

2.2. Characterizations. *2.2.1. Electrochemical Study.* Electrochemical studies were performed at room temperature on a CHI 730D electrochemical station (CH Instruments, Inc.) with a rotating disk electrode system (Pine Instrument, Grove City, PA) in a conventional three-electrode electrochemical system. The electrolyte was chosen to be a 0.1 M $HClO_4$ aqueous solution. Aaturated calomel electrode (SCE) and Pt foil were used as the reference and counter electrodes, respectively. A rotating disk electrode (RDE) with a glassy carbon disk (4 mm in diameter) was used as the working electrode. All electrode potentials are given versus the reversible hydrogen electrode (RHE).

The electrocatalyst slurry was prepared by sonicating 5 mg of electrocatalyst in a 2.5 mL mixture of 2-propanol and 5% Nafion solution for 20−30 min. Then a given volume of this

dx.doi.org/10.1021/jp401375b | J. Phys. Chem. C 2013, 117, 13413−13423

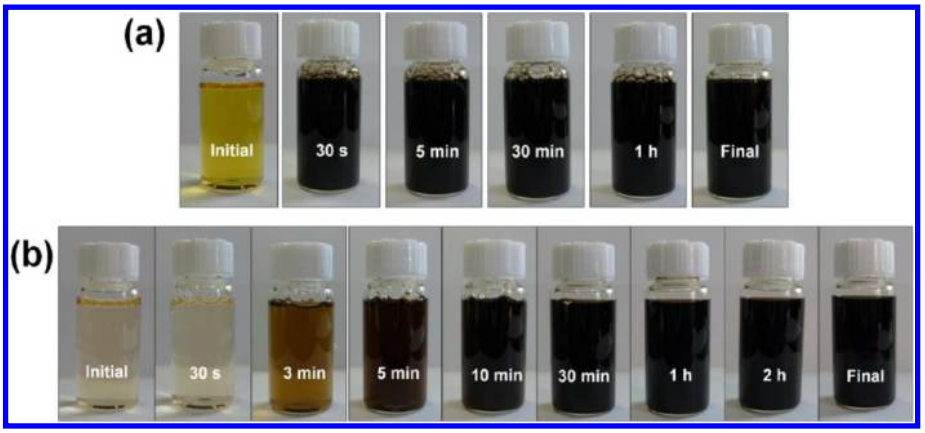

Figure 1. Photographs of reaction solutions reacted for different times in the preparation of (a) Pd and (b) Pt NCs. The solutions marked "Initial" were made by adding Na_2PdCl_4 or K_2PtCl_4 to water at the same concentration with the reaction solution except that Pluronic F127 copolymers were absent.

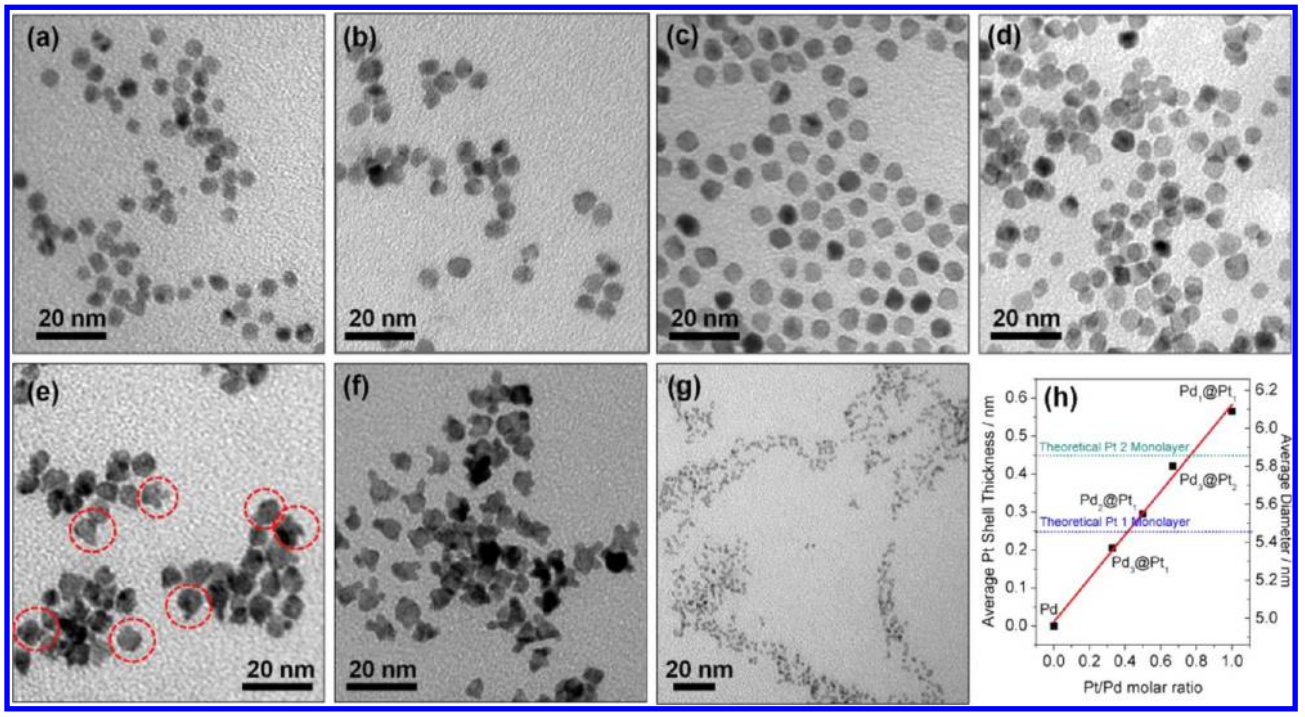

Figure 2. TEM images of (a) Pd, (b) $Pd_3@Pt_1$, (c) $Pd_2@Pt_1$, (d) $Pd_3@Pt_2$, (e) $Pd_1@Pt_1$, (f) $Pd_1@Pt_2$, and (g) Pt NCs. (h) Average Pt shell thickness and average particle diameter of Pd@Pt NCs as a function of the Pt/Pd molar ratio. The red circles in (e) mark several NCs having small Pt islands on the surface.

ink was dropped on the glassy carbon disk and allowed to dry in air at room temperature. For comparison, the commercial 20 wt % Pt/C catalysts (JM) were studied. The volume of ink dropped on the RDE is 6 μL for $Pd_3@Pt_1$/C, $Pd_2@Pt_1$/C, Pt/C(F127), and 20%Pt/C(JM); 5 μL for $Pd_1@Pt_1$/C, and 4 μL for $Pd_1@Pt_2$/C.

Before the electrochemical test, the potential of the working electrode was scanned between 0.06 and 1.26 V at 100 mV s^{-1} in a N_2-purged electrolyte several times to clean the surface of the catalysts. The cyclic voltammetry (CV) measurements were carried out in N_2-purged 0.1 M $HClO_4$ solutions at 50 mV s^{-1}. The specific electrochemical surface area (ECSA) is calculated from integrated hydrogen adsorption and desorption cyclic voltammograms using 0.21 mC cm_{Pt}^{-2} as the conversion factor. The ORR polarization curves were recorded positively at a sweep rate of 10 mV s^{-1} in O_2-saturated 0.1 M $HClO_4$ at room temperature and 1600 rpm. The kinetic current of the catalysts is calculated by using the well-known mass-transport correction for rotating disk electrodes: $j_k = j_d j/(j_d - j)$,[33] where j is the experimentally obtained current density, j_d the measured diffusion limiting current density, and j_k the mass-transport free kinetic current density. The kinetic data can be extracted by this equation in the region where $0.1j_d < j < 0.8j_d$.[34]

2.2.2. Single-Cell Testing. Fully humidified H_2 and O_2 at 65 °C and 150 kPa_{abs} were supplied to the anode and cathode, respectively. The single cell was conditioned at 1000 mA cm^{-2} for at least 10 h before polarization curves were recorded. The polarization curves were obtained at 65 °C at varying load current densities. Both the polarization curves and the internal resistance (IR) of the fuel cell (at 10 kHz) were measured by a Kikusui KFM-2030 FC impedance meter at the same time. After that, the cathode gas was switched to dry N_2 and the cell

dx.doi.org/10.1021/jp401375b | J. Phys. Chem. C 2013, 117, 13413−13423

was cooled to 30 °C. The cyclic voltammetry curves were recorded on a CHI-600C (CH Instruments, Inc.) with an anode as the counter and reference electrodes (dynamic hydrogen electrode, DHE), and the cathode was cycled between 0 and 1.0 V (vs DHE) at a sweep rate of 20 mV s^{-1} using fully humidified H_2 at the anode and dry N_2 at the cathode. The region corresponding to hydrogen desorption was used to measure the ECSA of the cathode using 0.21 mC cm_{Pt}^{-2} as a conversion factor. After that, the cathode gas was switched to fully humidified N_2 and the cell was heated back to 65 °C. The H_2 crossover current density was measured at 150 kPa_{abs} for H_2 pressure and 65 °C as described in the literature.[33]

The durability of cathode electrocatalysts was evaluated by cycling the cathode between 0.6 and 1.0 V (vs DHE) at a sweep rate of 50 mV s^{-1} at 65 °C. During potential cycling, the cell was fed with humidified H_2 (50 mL min^{-1}, 150 kPa_{abs}) at the anode and N_2 (40 mL min^{-1}, 150 kPa_{abs}) at the cathode.

2.2.3. Physical Characterizations. Transmission electron microscopy (TEM) images were taken using a JEOL JEM-2000EX electron microscope operating at 120 kV. The high-resolution TEM (HRTEM) and high-angle annular dark-field scanning TEM (HAADF-STEM) analyses were performed on an FEI Tecnai G2 F30 microscope. X-ray diffraction (XRD) analysis was conducted on a Rigaku D/MAX-2500/PC X-ray diffractometer using Cu Kα radiation (λ = 0.154 056 nm). UV−vis spectra were recorded on a Shimadzu UV2550 spectrometer. Transmission infrared spectra were collected in the transmission mode on a Bruker Tensor 27 Fourier transform infrared (FT-IR) spectrometer. TGA was tested by using a TGA analyzer (Mettler Toledo TGA/SDTA851e) from room temperature at a heating rate of 10 °C min^{-1} under air flow. X-ray photoelectron spectra were obtained from an ESCALAB 250Xi (Thermo Scientific) spectrometer using Al Kα radiation. The composition of the catalysts was determined by ICP-AES (Perkin-Elmer Optima 2000 DV).

3. RESULTS AND DISCUSSION

3.1. Structural Analysis. The Pd@Pt NCs were prepared by a one-pot sequential reduction process. First, Na_2PdCl_4 aqueous solution was added to the Pluronic F127 solution, and the color of the reaction solution immediately changed to dark black. This color remained the same in the subsequent reaction process (Figure 1a), implying the high reducing ability of F127 toward $PdCl_4^{2-}$. The UV−vis measurements showed that the adsorption peak for Na_2PdCl_4 disappeared after reaction at 80 °C for 2 h, proving the reduction of Na_2PdCl_4 by F127 (Figure S1, Supporting Information). As reported previously, PEO segments in PEO−PPO−PEO triblock copolymers had a reducing capacity toward metal ions, and they can form cavities (pseudocrown ethers) that bind $PdCl_4^{2-}$. The bound $PdCl_4^{2-}$ ions may be reduced via oxidation of the oxyethylene segments by the metal center.[35,36] TEM measurement showed that nearly spherical Pd NCs (Figure 2a) with an average particle size of 4.96 nm (Figure S2a, Supporting Information) were obtained. According to Wulff's theorem, the Pd NC with an fcc structure tends to evolve into a truncated octahedral shape to hold the smallest surface area and minimum surface energy for a given volume.[27] Actually, a truncated octahedron has a nearly spherical profile in the low-magnified TEM image as shown in Figure 2a. These Pd NCs were used as seeds for the overgrowth of Pt via injecting a given amount of K_2PtCl_4 aqueous solution into the Pd colloid solution; then $PtCl_4^{2-}$ ions were reduced by F127 and Pt atoms deposited on the Pd NCs. After another 3 h, Pd@Pt NCs (denoted as $Pd_3@Pt_1$, $Pd_2@Pt_1$, $Pd_3@Pt_2$, $Pd_1@Pt_1$, and $Pd_1@Pt_2$ for the corresponding Pt/Pd molar ratio) were obtained. The adsorption peak for K_2PtCl_4 in the UV−vis spectrum disappeared in the final colloid solutions (Figure S1). Moreover, the Pt/Pd molar ratio of the final products measured by ICP was very close to the nominal value (Table 1), further indicating the reducing ability of F127 copolymers toward both $PdCl_4^{2-}$ and $PtCl_4^{2-}$ ions.

Table 1. Pt/Pd Molar Ratio of Different Pd@Pt NCs

NCs	Pt/Pd molar ratio by ICP	Pt/Pd molar ratio by XPS
$Pd_3@Pt_1$	27/73	41/59
$Pd_2@Pt_1$	37/63	52/48
$Pd_3@Pt_2$	41/59	51/49
$Pd_1@Pt_1$	54/46	71/29
$Pd_1@Pt_2$	65/35	78/22

The as-prepared NCs could be loaded onto carbon blacks (Vulcan XC-72R) to make supported NCs. The actual metal loading of these catalysts shown in Table 2 is close to the nominal loading, proving the effectiveness of the catalyst preparation method. The XRD patterns of 20%Pt/C(JM), Pd/C, $Pd_3@Pt_1$/C, $Pd_2@Pt_1$/C, $Pd_1@Pt_1$/C, and $Pd_1@Pt_2$/C are shown in Figure S3 (Supporting Information). The diffraction peak at around 25° comes from the carbon black, while the diffraction peaks of the six catalysts at around 40°, 47°, 68°, 81°, and 86° are attributed to the (111), (200), (220), (311), and (222) planes of the fcc structure of Pt and Pd, respectively, suggesting good crystallinity of these homemade Pd@Pt NCs. Because Pt and Pd have the same crystal structure (fcc) and very close lattice parameters, the sets of diffraction peaks of Pt and Pd are overlapped.[5,8]

Table 2. Metal Loading, Initial Specific ECSA, Retention Percentage of ECSA, and Pt/Pd Molar Ratio after Degradation for Different Catalysts

catalyst	metal loading, wt %	specific ECSA, $m^2\ g_{Pt}^{-1}$	retention of ECSA after degradation,[a] %	Pt/Pd molar ratio after degradation[a]
20%Pt/C(JM)	21.9	80.6	65.0	na
$Pd_3@Pt_1$/C	28.8	111.0	80.1	37/63
$Pd_2@Pt_1$/C	30.7	83.6	81.0	32/68
$Pd_1@Pt_1$/C	42.3	57.8	83.2	51/49
$Pd_1@Pt_2$/C	54.3	30.6	76.3	68/32

[a]The degradation was carried out by cycling the catalyst between 0.6 and 1.1 V (RHE) at 50 mV s^{-1} for 2000 cycles in N_2-purged 0.1 M $HClO_4$.

The morphology of Pd@Pt NCs was characterized by TEM. As shown in Figure 2b−d, $Pd_3@Pt_1$, $Pd_2@Pt_1$, and $Pd_3@Pt_2$ NCs are quasi-spheres with smooth surfaces like Pd NCs. In contrast, the surfaces of $Pd_1@Pt_1$ NCs are slightly rough with small Pt islands on some NCs (see Figure 2e and Figure S4 (Supporting Information) for more examples), while nearly all $Pd_1@Pt_2$ NCs have longer Pt branches (Figure 2f). The average particle diameter was 5.37, 5.55, 5.80, and 6.09 nm for $Pd_3@Pt_1$, $Pd_2@Pt_1$, $Pd_3@Pt_2$, and $Pd_1@Pt_1$ NCs, respectively (Figure S2, Supporting Information), and it increased linearly with the

dx.doi.org/10.1021/jp401375b | J. Phys. Chem. C 2013, 117, 13413−13423

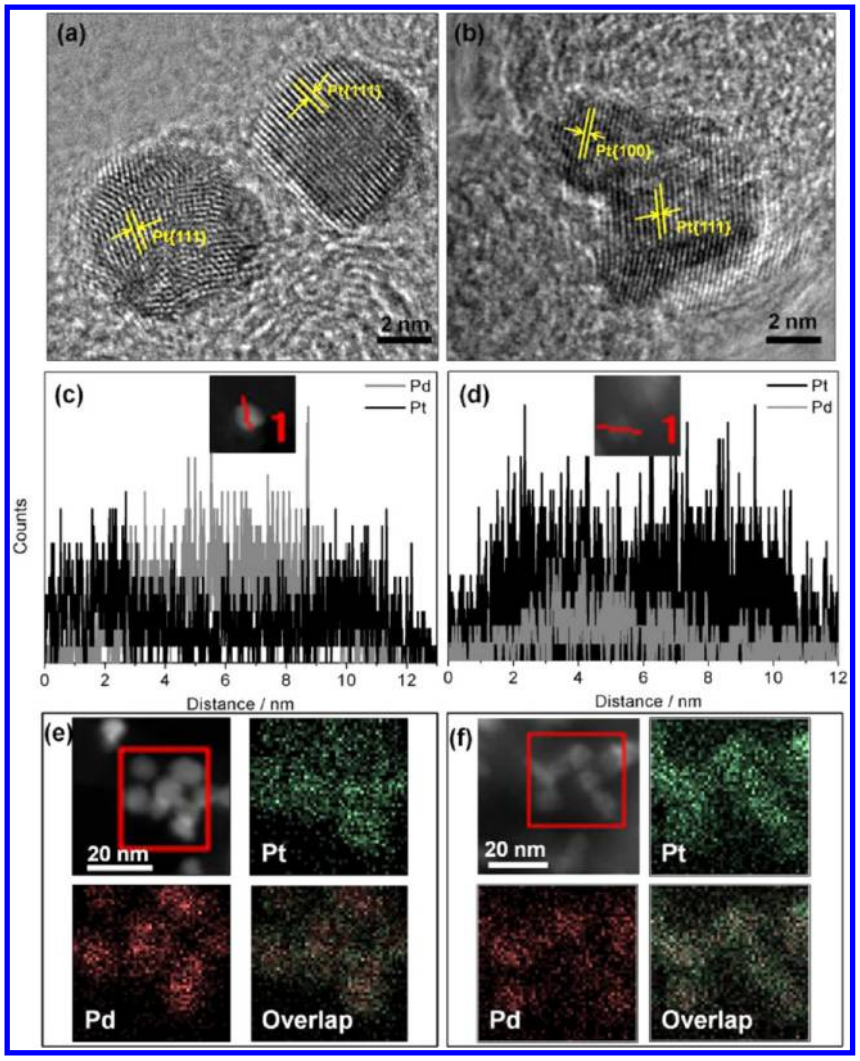

Figure 3. (a, b) HRTEM images, (c, d) cross-sectional compositional line profiles, and (e, f) HAADF-STEM−EDX mapping images of $Pd_2@Pt_1$ (left panels) and $Pd_1@Pt_2$ (right panels) NCs.

Pt/Pd molar ratio (Figure 2h). Due to the branched morphology, the Pt shell thickness of $Pd_1@Pt_2$ NCs was not evaluated. As a result, it was reasonable to consider that Pt was deposited on the surface of Pd NCs. We further characterized the $Pd_2@Pt_1$ and $Pd_1@Pt_2$ NCs by HRTEM. The spherical and branched morphology of $Pd_2@Pt_1$ and $Pd_1@Pt_2$ NCs could be distinctly recognized in parts a and b, respectively, of Figure 3. Moreover, the lattice fringes displayed in Figure 3a,b proved the crystalline nature of Pd@Pt NCs. The elemental distributions of Pd and Pt in the NCs were analyzed by high-angle annular dark field scanning TEM (HAADF-STEM). The energy-dispersive X-ray (EDX) spectra of a randomly selected $Pd_2@Pt_1$ or $Pd_1@Pt_2$ NC (Figure S5, Supporting Information) show that it is composed of Pt and Pd elements. Furthermore, the elemental line profiles (Figure 3c,d) and maps (Figure 3e,f) definitely reveal that the NCs consist of a Pd core and Pt shell.

As surface-sensitive techniques, X-ray photoelectron spectroscopy (XPS) and CV were applied to further analyze the surface of different NCs. The near surface composition of catalysts can be evaluated by XPS.[37−39] As shown in Table 1, the near surface Pt/Pd molar ratios for all Pd@Pt NCs are noticeably higher than the bulk Pt/Pd molar ratios measured by ICP, revealing a Pt-dominating surface composition for Pd@Pt NCs. Furthermore, a slight negative shift in the Pt binding energy was observed in the XPS spectrum of Pd@Pt NCs as compared with 20%Pt/C(JM) (Figure 4 and Figure S6, Supporting Information), which may be ascribed to the larger electronegativity of Pt (2.28) than that of Pd (2.20).[40,41]

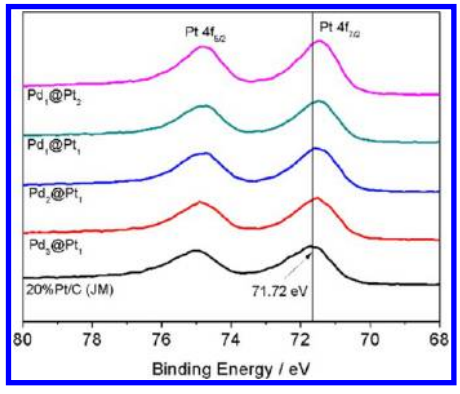

Figure 4. XPS spectra of 20%Pt/C(JM) and Pd@Pt NCs with different Pt/Pd molar ratios. The binding energy of Pt $4f_{7/2}$ for 20%Pt/C(JM) is 71.72 eV, which has been marked in the figure. The corresponding deconvoluted spectra of these catalysts are plotted in Figure S6 (Supporting Information).

dx.doi.org/10.1021/jp401375b | J. Phys. Chem. C 2013, 117, 13413−13423

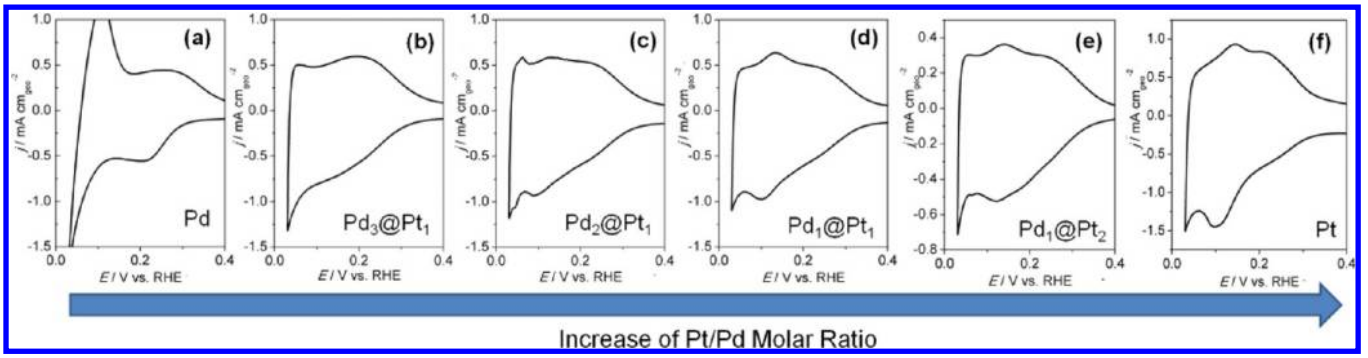

Figure 5. Cyclic voltammetry curves for the carbon-supported (a) Pd, (b) $Pd_3@Pt_1$, (c) $Pd_2@Pt_1$, (d) $Pd_1@Pt_1$, and (e) $Pd_1@Pt_2$ NCs and (f) 20% Pt/C(JM) in N_2-purged 0.1 M $HClO_4$ at 50 mV s^{-1}.

Scheme 1. Synthesis of Pd–Pt Bimetallic NCs Consisting of a Pd Core and a Pt Shell with Different Pt/Pd Molar Ratios

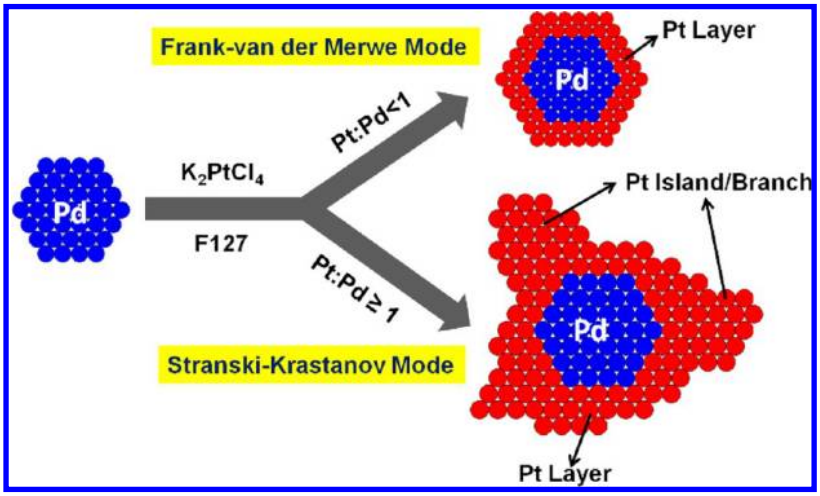

Moreover, on the CV curves obtained in 0.1 M $HClO_4$ (Figure 5), it is found that the CV curves of all Pd@Pt NCs are different from those of Pd NCs, confirming the successful modification of Pt on the surface of Pd. Furthermore, with an increase of the Pt/Pd molar ratio, the curve shape of the hydrogen adsorption/desorption region (0–0.4 V vs RHE) of Pd@Pt/C gradually evolves to a shape that resembles that of Pt/C, indicating an increase of the Pt shell thickness and compactness. As expected, the Pt mass-based specific ECSA was reduced with an increase of the Pt/Pd molar ratio (Table 2) owing to the gradual increase of the Pt shell thickness. The above results undoubtedly confirm the core–shell structure of Pd@Pt NCs.

The deposition of Pt on the surface of Pd instead of homogeneous nucleation in the solution may be caused by the relatively weaker reducing ability of F127 toward K_2PtCl_4. This was visually evidenced by the slow color change in the preparation of Pt NCs (Figure 1b). When K_2PtCl_4 is added to the Pd colloid, $PtCl_4^{2-}$ ions cannot be reduced by F127 immediately. Because the heterogeneous nucleation is thermodynamically proved in comparison with homogeneous nucleation,[4] $PtCl_4^{2-}$ ions will be prone to be reduced on the surface of Pd, resulting in core–shell Pd@Pt NCs instead of pure Pt NCs in the solution.

On the basis of thermodynamics, the growth mode of Pt on the Pd surface can be determined by the Gibbs surface energy change (ΔG) during the deposition according to the following equation:[4]

$$\Delta G = \gamma_{Pt} + \gamma_i + \gamma_s - \gamma_{Pd}$$

where γ_{Pt} and γ_{Pd} are the specific surface energies of Pt and Pd, respectively, γ_i is the specific interfacial energy between Pt and Pd, and γ_s is the strain energy caused by the mismatch between Pt and Pd. Generally, thermodynamics predict an island growth mode for Pt deposition on a Pd surface ($\Delta G > 0$), because γ_{Pt} is higher relative to γ_{Pd} and Pt attempts to form islands to minimize the interfacial area shared with Pd.[3,21] However, we found that the surfaces of $Pd_3@Pt_1$, $Pd_2@Pt_1$, and $Pd_3@Pt_2$ NCs were smooth without islands (Figure 2). Therefore, it is considered that Pt could grow on the Pd surface by the layer-by-layer growth mode (i.e., Frank–van der Merwe growth mode) using F127 as the reductant, stabilizer, and capping agent simultaneously at low Pt/Pd molar ratio (Pt/Pd molar ratio <1) (Scheme 1).[4] During the reaction, the F127 might adsorb on the Pd core through the interaction between the hydrophobic PPO segments and Pd surface, while the hydrophilic PEO segments would reduce the $PtCl_4^{2-}$. The obtained Pt atoms were then deposited on the Pd surface and protected by F127, which decreased the surface energy of Pt (γ_{Pt}). Moreover, the quite small lattice mismatch between Pd and Pt (0.77%)[19] results in small γ_i and γ_s. Hence, layer-by-layer growth could be realized ($\Delta G < 0$). The average Pt shell thickness estimated by measuring the diameter difference between the Pd@Pt NCs and the seeded Pd NCs was 0.205, 0.295, and 0.420 nm for $Pd_3@Pt_1$, $Pd_2@Pt_1$, and $Pd_3@Pt_2$ NCs, respectively. According to the literature,[42] the particle size will be increased by ~0.225 nm for every Pt monolayer (ML)

dx.doi.org/10.1021/jp401375b | J. Phys. Chem. C 2013, 117, 13413–13423

deposited on the surface of Pd. As a result, a near ML shell and a 2 ML Pt shell were formed on the surface of the Pd core for $Pd_2@Pt_1$ and $Pd_3@Pt_2$ NCs, respectively. Interestingly, at a high Pt/Pd molar ratio (1/1 and 2/1), the surface of NCs is modified with Pt islands (Figure 2). On the basis of CV results (Figure 5), these Pt islands did not directly grow on the Pd core, because in that case part of the Pd core surfaces would be exposed, resulting in the appearance of intense peaks for hydrogen adsorption and desorption on the CV curves due to the diffusion of hydrogen atoms into the lattice of Pd.[5,7] On the contrary, it was believed that Pt islands were deposited on the preformed compact Pt layers around the Pd core; i.e., this is the island-on-wetting-layer growth mode (i.e., Stranski–Krastanov growth mode) (Scheme 1) .[4] The transformation of the growth mode from layer-by-layer to island-on-wetting-layer might be caused by the increased strain energy (γ_s) with the growth of Pt layers, with the large strain energy having to be released by a change of the growth mode.[4] The average Pt shell thickness for $Pd_1@Pt_1$ NCs was evaluated to be 0.565 nm, larger than the 2 ML Pt shell but smaller than the 3 ML Pt shell. As a result, the Pt islands may start to form after the deposition of the 2 ML Pt shell, and Pt islands further grow to branches with an increase of the Pt/Pd molar ratio to 2/1 (Scheme 1). Additionally, the Pt islands may selectively nucleate on some sites with high surface energy in an attempt to minimize the total free energy; thus, it can be found in Figure 2f that the $Pd_1@Pt_2$ NCs only had a couple of Pt branches.

As an electrocatalyst, the clean surface exposed is of significant importance. The FT-IR spectra and TGA curves of Pd@Pt NCs and Pluronic F127 are displayed in Figure 6. It is observed that the FT-IR curve of Pd@Pt NCs did not show the typical characteristic peaks related to F127 (Figure 6a).

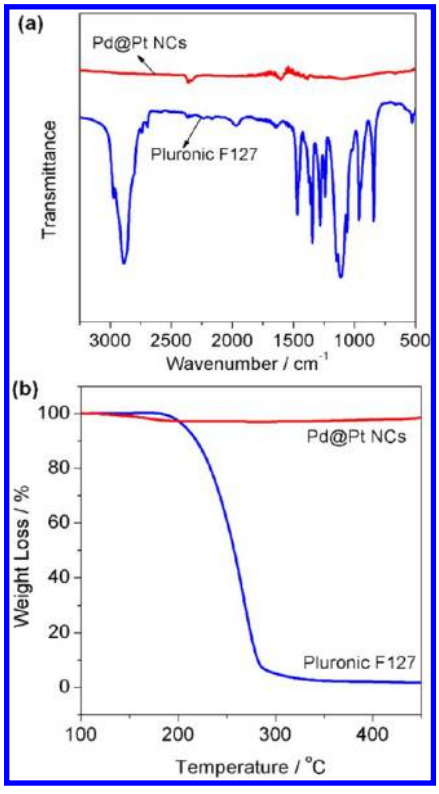

Figure 6. (a) FT-IR spectra and (b) TGA curves of Pluronic F127 and $Pd_2@Pt_1$ NCs.

Moreover, there is very little weight loss of Pd@Pt NCs under the whole temperature range in comparison with F127 (Figure 6b). The FT-IR and TGA measurements proved that the F127 copolymer could be easily removed from the surface of NCs by washing with ethanol and water several times and the Pd@Pt NCs had a nearly clean surface.

3.2. Catalytic Performance toward Oxygen Reduction Reaction. The electrocatalytic performances of Pt and Pd@Pt NCs toward ORR were investigated and compared with that of the state-of-the-art 20%Pt/C(JM) catalyst in 0.1 M $HClO_4$ at room temperature. It is shown in Figure S7 (Supporting Information) that the CV and ORR activity for Pt/C(F127) was nearly identical with that of 20%Pt/C(JM) because the Pt particle size and distribution of Pt particles on the carbon black were similar for both of the catalysts (Figure 2g; Figures S2f, S7, and S8, Supporting Information). Furthermore, the ORR polarization curves for different Pd@Pt/C catalysts are presented in Figure 7a; the area-specific activity (ASA) and Pt mass activity (MA) obtained by normalizing the kinetic current densities against the ECSA and Pt mass of these catalysts are compared in parts b and c, respectively, of Figure 7. It can be found that the ASA of Pd@Pt NCs for every molar ratio of Pt/Pd was larger than that of 20%Pt/C(JM). It is accepted that the oxygen reduction on the surface of Pt-based catalysts was mainly affected by coverage of the intermediate products of ORR (oxygenated species, denoted as OH_{ad}), which block active sites for O_2 adsorption and thus inhibit the ORR kinetics.[43−45] The catalyst which can accelerate the desorption of OH_{ad} will present enhanced ORR activity. The improvement of the ASA of Pd@Pt NCs may be caused by the weaker adsorption of OH_{ad} on the surface of Pt, which is reflected in the CV curves, where the peak potential of surface oxide reduction was shifted positively from 0.747 V for 20%Pt/C(JM) to around 0.802 V for Pd@Pt NCs (Figure S9, Supporting Informaiton). It is supposed that the fraction of edge/corner atoms in total surface atoms declines with an increase of the size of the nanoparticles,[42,46] and these low-coordinated edge/corner atoms possess larger binding energy toward OH_{ad}, which is negative in the ORR kinetics.[14,44] As a result, the Pt shell deposited on the ∼5 nm Pd NC may possess a smaller number of edge/corner atoms than that of Pt nanoparticles (1.5−4.0 nm, Figure S8a) of 20%Pt/C(JM), giving rise to an improved ASA for ORR. Moreover, with an increase of the Pt/Pd molar ratio, the compactness of the Pt shell was improved (Figure 5) and the faceted morphology of Pd@Pt NCs became more remarkable (Figure 2), which led to a further enhancement of ASA.[14] Particularly, $Pd_1@Pt_2$ NCs having a branched Pt shell showed the highest ASA, 2.7 times that of 20%Pt/C(JM) at 0.9 V (vs RHE) (Figure 7d), which may result from the branched morphology of the Pt shell, because the branched Pt NCs were reported to display an enhanced ASA in ORR.[7,43,47] However, the MA of $Pd_1@Pt_2$ NCs was low due to the small specific ECSA (Table 2), i.e., low utilization of Pt atoms. In comparison, $Pd_2@Pt_1$ NCs showed the best MA (0.37 A mg_{Pt}^{-1}), which was 2.3 times that of 20% Pt/C(JM) (0.16 A mg_{Pt}^{-1}) and also greater than that of recently reported Pt-on-Pd nanostructures (0.14 A mg_{Pt}^{-1} at 0.9 V),[8] Pd−Pt nanodendrites (0.241 ± 0.013 A mg_{Pt}^{-1} at 0.9 V),[7] AgPd@Pt core−shell NCs (0.23 A mg_{Pt}^{-1} at 0.9 V),[41] and Pt−Pd hollow octahedral nanocages (∼1.2 A mg_{Pt}^{-1} at 0.85 V vs 1.9 A mg_{Pt}^{-1} for $Pd_2@Pt_1/C$ at 0.85 V in this work).[48]

Furthermore, the long-term stability of Pd@Pt NCs was evaluated by applying linear potential cycling between 0.6 and

dx.doi.org/10.1021/jp401375b | J. Phys. Chem. C 2013, 117, 13413−13423

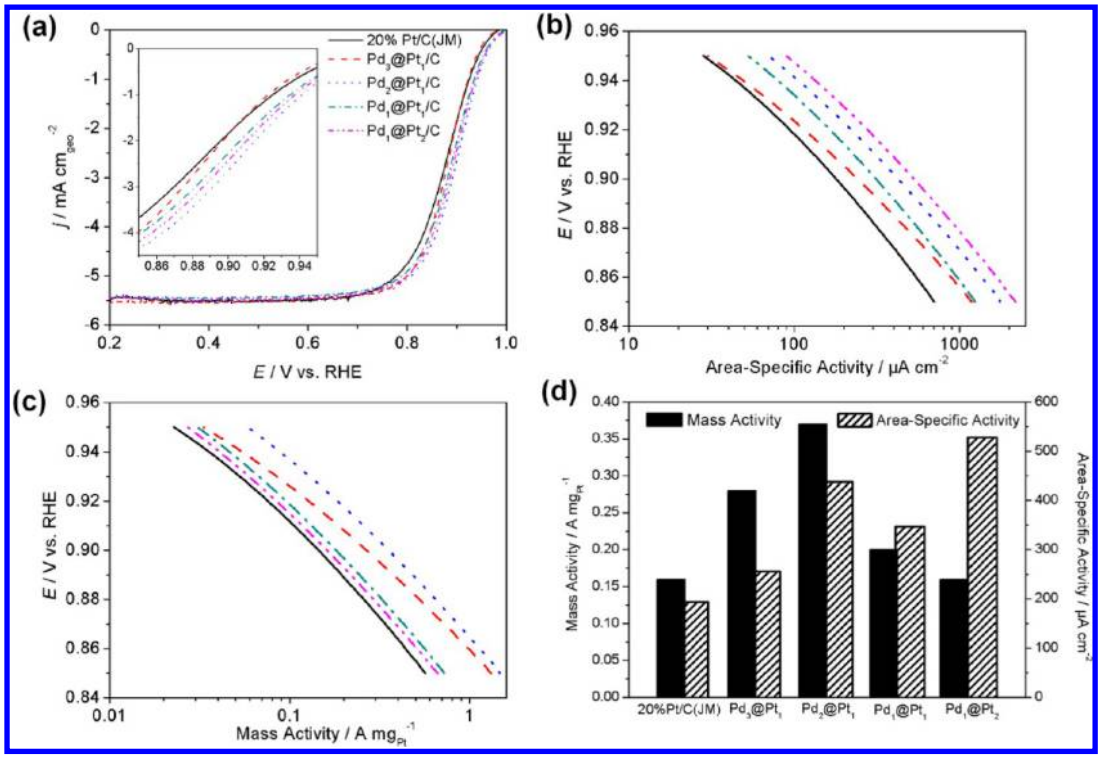

Figure 7. (a) ORR polarization curves for Pd@Pt/C and commercial Pt/C catalysts in O_2-saturated 0.1 M $HClO_4$. The inset shows the region between 0.95 and 0.85 V (vs RHE). (b, c) ASA and MA given as kinetic current densities normalized against the ECSA and Pt mass of these catalysts, respectively. (d) MA and ASA at 0.9 V (vs RHE) for these catalysts.

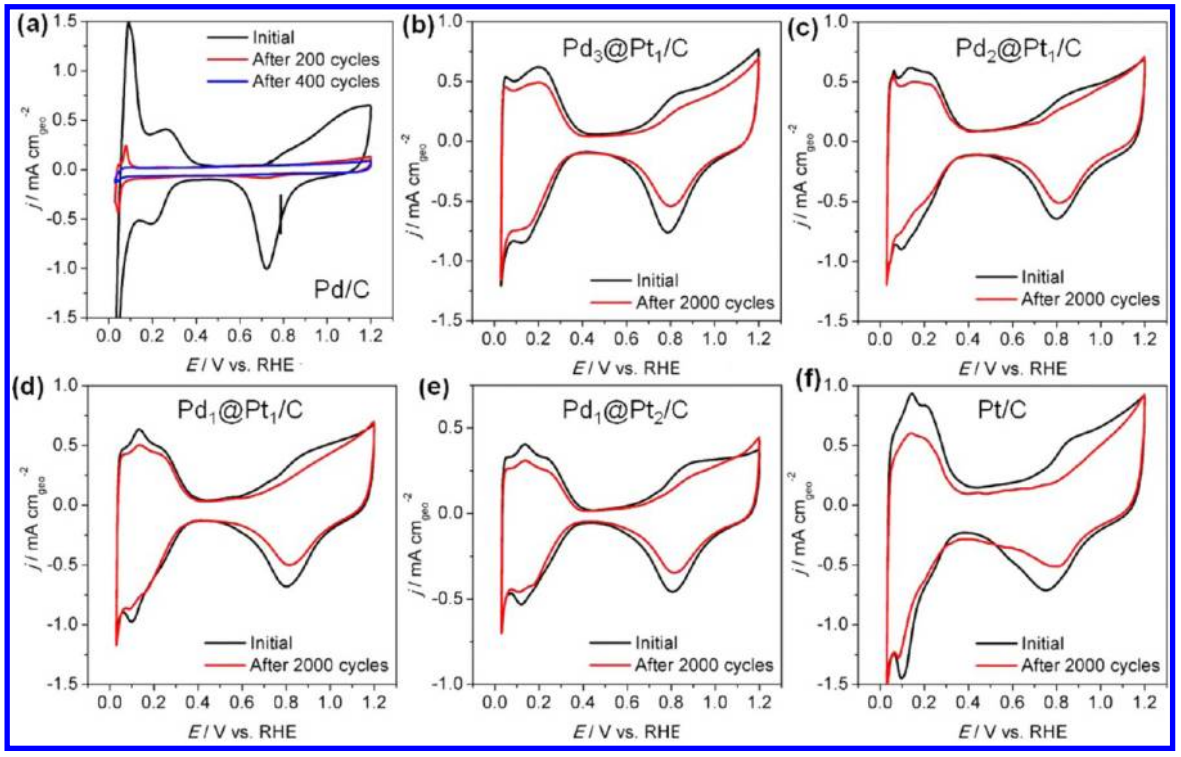

Figure 8. CV curves of (a) Pd/C, (b) $Pd_3@Pt_1/C$, (c) $Pd_2@Pt_1/C$, (d) $Pd_1@Pt_1/C$, (e) $Pd_1@Pt_2/C$, and (f) 20%Pt/C(JM) before and after potential cycling between 0.6 and 1.1 V in N_2-purged 0.1 M $HClO_4$.

1.1 V in N_2-purged 0.1 M $HClO_4$, and the CV curves before and after degradation are shown in Figure 8. After 2000 cycles, the loss of initial ECSA for all Pd@Pt/C catalysts was only around 20% (Table 2), whereas the Pd was completely dissolved for Pd/C after only 400 cycles. Moreover, the Pt/Pd molar ratio after degradation (Table 1) was very close to the initial value except for $Pd_3@Pt_1/C$, implying that the dissolution of the Pd core could be avoided by the protection

dx.doi.org/10.1021/jp401375b | J. Phys. Chem. C 2013, 117, 13413−13423

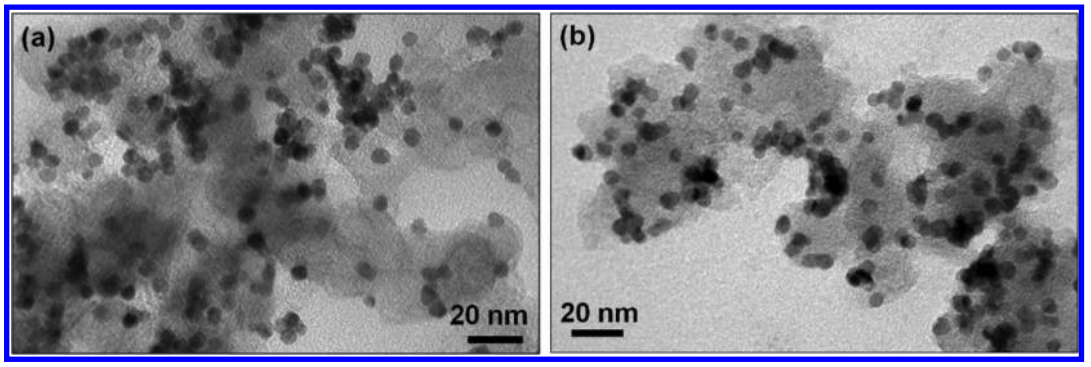

Figure 9. TEM images of $Pd_2@Pt_1/C$ (a) before and (b) after 2000 cycles between 0.6 and 1.1 V in N_2-purged 0.1 M $HClO_4$.

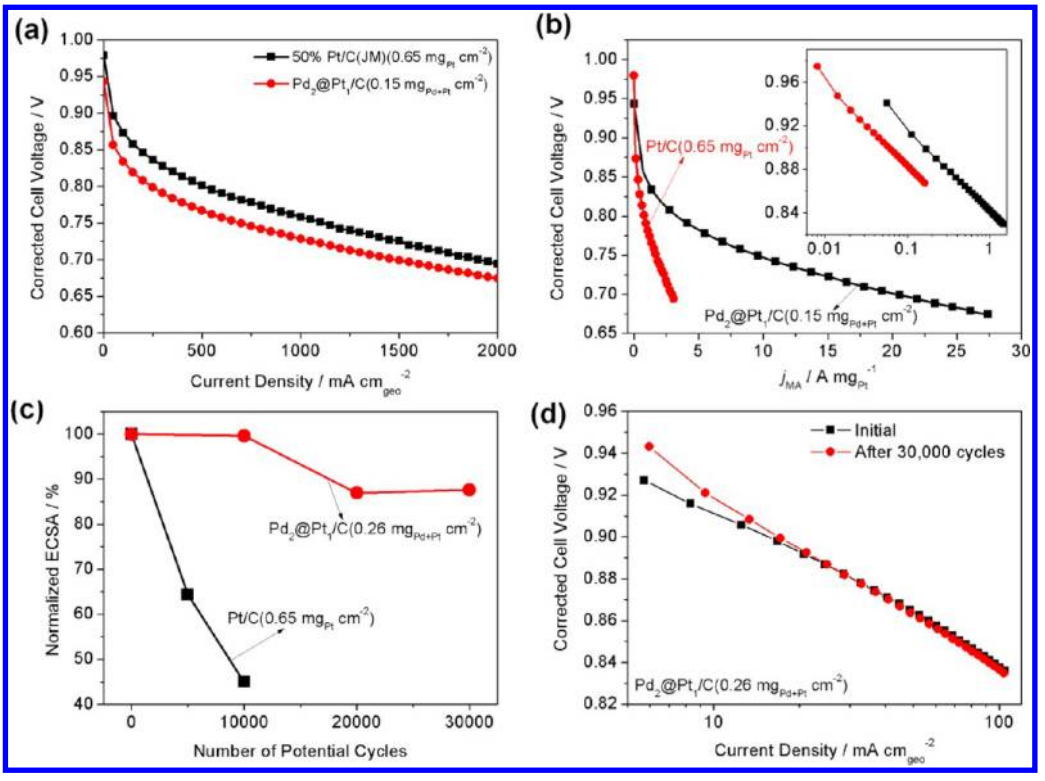

Figure 10. (a) Polarization curves of single H_2/O_2 fuel cells using $Pd_2@Pt_1/C$ or 50%Pt/C(JM) cathode catalysts. (b) Comparison of the mass activity of cathode catalysts shown in (a). The inset shows the Tafel plots under low current densities. (c) Normalized ECSA of $Pd_2@Pt_1/C$ and Pt/C cathode catalysts after different potential cycles between 0.6 and 1.0 V (vs DHE) at 65 °C. (d) Tafel plots for the single cell using a $Pd_2@Pt_1/C$ cathode catalyst before and after 30 000 potential cycles. The metal loading shown in this figure is cathode metal loading. The polarization curves were tested at 65 °C with 100% humidified H_2/O_2 at 150 kPa_{abs}, and the cell voltage is that after IR and H_2 crossover correction.

of the compact Pt shell, while the Pd core of $Pd_3@Pt_1$ NCs was lost to some extent probably due to the less compact Pt shell. Furthermore, taking $Pd_2@Pt_1$ NCs as an example, the particle morphology and size nearly did not change after the accelerated tests (Figure 9 and Figure S10, Supporting Information). In sharp contrast, the ECSA loss for Pt/C was 35% after 2000 cycles, and the particle size was increased from 2.47 to 3.23 nm with a 28% increment (Figure S8, Supporting Information).

Single-fuel-cell testing was performed on 5 cm^2 catalyst-coated membrane (CCM) electrodes. $Pd_2@Pt_1/C$ and commercial 50 wt % Pt/C were compared as the cathode catalyst. The purpose of development of core−shell catalysts was to lower the loading of Pt on the cathode; thus, an MEA with a low metal loading of 0.15 mg_{Pd+Pt} cm^{-2} (i.e., 0.073 mg_{Pt} cm^{-2}) on the cathode was fabricated to test the performance of $Pd_2@Pt_1/C$. After IR and H_2 crossover correction, the cell voltage of the MEA with $Pd_2@Pt_1/C$ cathodic catalysts is only less than 50 mV relative to that of MEA with a cathode made by Pt/C catalysts (0.65 mg_{Pt} cm^{-2}) throughout the whole current range on the polarization curves (Figure 10a). The Pt mass activities of $Pd_2@Pt_1/C$ and Pt/C are compared in Figure 10b. The Pt mass activity at 0.9 V for Pt/C is 0.059 A mg_{Pt}^{-1}, which is close to the reported Pt/C activity in a fuel cell under similar conditions.[49] In comparison, the activity for $Pd_2@Pt_1/C$ is 0.166 A mg_{Pt}^{-1}, nearly 3 times that of Pt/C, and this improvement factor was increased to 4.5 at 0.75 V (9.59 A mg_{Pt}^{-1} for $Pd_2@Pt_1/C$ vs 2.15 A mg_{Pt}^{-1} for Pt/C), indicating that $Pd_2@Pt_1/C$ catalysts also possessed outstanding activity in the practical working conditions of PEMFCs. Furthermore, when the metal loading of $Pd_2@Pt_1/C$ was increased to 0.62 mg_{Pd+Pt} cm^{-2}, the fuel cell with $Pd_2@Pt_1/C$ could show a performance similar to that of the fuel cell using Pt/C (0.65

dx.doi.org/10.1021/jp401375b | J. Phys. Chem. C 2013, 117, 13413−13423

mg_{Pt} cm^{-2}) (Figure S11, Supporting Information). Moreover, nearly identical polarization curves could also be obtained for $Pd_2@Pt_1/C$ and Pt/C with cathode metal loadings of 0.26 mg_{Pd+Pt} cm^{-2} and 0.26 mg_{Pt} cm^{-2}, respectively (Figure S11). On the basis of the above results, $Pd_2@Pt_1/C$ catalysts may give us a hopeful pathway to achieve the target of reducing the Pt loading on the cathode.

Additionally, $Pd_2@Pt_1/C$ presented superior durability to potential cycling in the single fuel cell. As shown in Figure 10c, the ECSA loss for $Pd_2@Pt_1/C$ was only 13% after 30 000 potential cycles between 0.6 and 1.0 V (vs DHE) at 65 °C. In sharp contrast, the loss was 55% for Pt/C after only 10 000 cycles. Moreover, the degradation of the cell performance with $Pd_2@Pt_1/C$ cathode catalysts was scarcely observed under low current densities (Figure 10d) in which the activity of the catalysts can be reflected in exclusion of the degradation of other MEA components and the influence of reactant transport. The above results demonstrate superior performance of $Pd_2@Pt_1/C$ in the fuel cell working conditions and indicate Pd@Pt NCs are promising candidates for utilization in practice.

4. CONCLUSIONS

A novel, facile and green method was demonstrated here for the synthesis of core−shell-structured sub 10 nm Pd@Pt NCs with controlled morphology using commercially available PEO−PPO−PEO amphiphilic triblock copolymers as the reductant, stabilizer, and capping agent in aqueous solutions. Pt overgrew on the Pd surface by a layer-by-layer or island-on-wetting-layer growth mode, which could be adjusted simply by the Pt/Pd molar ratio, resulting in different Pt shell morphologies. A compact and smooth Pt shell with a near-monolayer thickness was obtained on $Pd_2@Pt_1$ NCs, while a branched Pt shell was obtained on $Pd_1@Pt_2$ NCs, which showed the best MA and ASA for ORR relative to those of Pt/C. Furthermore, $Pd_2@Pt_1$ NCs presented superior activity and durability in single-cell testing at very low Pt loading. Thereby, the efficiency of Pt was remarkably enhanced, leading to a sharply reduced cost, which is very valuable for practical use in fuel cells. Besides, these Pd@Pt NCs may find uses in the application of automotive catalytic converters, gas sensors, petroleum refining, and hydrogen production. This novel synthesis method offers the advantages of aqueous-phase synthesis, low cost, large-scale production, and high electrocatalytic performance. Furthermore, the method reported here can be used to prepare other monometallic, bimetallic, or even multimetallic nanocrystals with well-defined shapes and composition distributions for catalysis and other applications.

■ ASSOCIATED CONTENT

Supporting Information

UV−vis spectra, particle size distribution, XRD spectra, EDX spectra, deconvoluted Pt 4f XPS spectra, electrochemical properties of Pt/C(F127), particle size change before and after degradation for 20%Pt/C(JM), comparison of CV curves of different catalysts, and polarization curves of fuel cells with different metal loadings. This material is available free of charge via the Internet at http://pubs.acs.org."

■ AUTHOR INFORMATION

Corresponding Author

*Phone: +86 411 84379153. Fax: +86 411 84379185. E-mail: zhgshao@dicp.ac.cn.

Notes

The authors declare no competing financial interest.

■ ACKNOWLEDGMENTS

This work was financially supported by the National High Technology Research and Development Program of China (Grant Nos. 2011AA11A273 and 2011AA050701) and the National Natural Science Foundations of China (Grant Nos. 21076208 and 20936008).

■ REFERENCES

(1) Ferrando, R.; Jellinek, J.; Johnston, R. L. Nanoalloys: From Theory to Applications of Alloy Clusters and Nanoparticles. *Chem. Rev.* **2008**, *108*, 845−910.

(2) Yuan, Q.; Wang, X. Aqueous-Based Route toward Noble Metal Nanocrystals: Morphology-Controlled Synthesis and Their Applications. *Nanoscale* **2010**, *2*, 2328−2335.

(3) Carbonea, L.; Cozzoli, P. D. Colloidal Heterostructured Nanocrystals: Synthesis and Growth Mechanisms. *Nano Today* **2010**, *5*, 449−493.

(4) Peng, Z. M.; Yang, H. Designer Platinum Nanoparticles: Control of Shape, Composition in Alloy, Nanostructure and Electrocatalytic Property. *Nano Today* **2009**, *4*, 143−164.

(5) Zhang, H.; Yin, Y. J.; Hu, Y. J.; Li, C. Y.; Wu, P.; Wei, S. H.; Cai, C. X. Pd@Pt Core−Shell Nanostructures with Controllable Composition Synthesized by a Microwave Method and Their Enhanced Electrocatalytic Activity toward Oxygen Reduction and Methanol Oxidation. *J. Phys. Chem. C* **2010**, *114*, 11861−11867.

(6) Liu, L.; Samjeske, G.; Nagamatsu, S.-i.; Sekizawa, O.; Nagasawa, K.; Takao, S.; Imaizumi, Y.; Yamamoto, T.; Uruga, T.; Iwasawa, Y. Enhanced Oxygen Reduction Reaction Activity and Characterization of Pt−Pd/C Bimetallic Fuel Cell Catalysts with Pt-Enriched Surfaces in Acid Media. *J. Phys. Chem. C* **2012**, *116*, 23453−23464.

(7) Lim, B.; Jiang, M. J.; Camargo, P. H. C.; Cho, E. C.; Tao, J.; Lu, X. M.; Zhu, Y. M.; Xia, Y. A. Pd−Pt Bimetallic Nanodendrites with High Activity for Oxygen Reduction. *Science* **2009**, *324*, 1302−1305.

(8) Peng, Z. M.; Yang, H. Synthesis and Oxygen Reduction Electrocatalytic Property of Pt-on-Pd Bimetallic Heteronanostructures. *J. Am. Chem. Soc.* **2009**, *131*, 7542−7543.

(9) Sasaki, K.; Naohara, H.; Cai, Y.; Choi, Y. M.; Liu, P.; Vukmirovic, M. B.; Wang, J. X.; Adzic, R. R. Core-Protected Platinum Monolayer Shell High-Stability Electrocatalysts for Fuel-Cell Cathodes. *Angew. Chem., Int. Ed.* **2010**, *49*, 8602−8607.

(10) Wang, Y.; Chen, K. S.; Mishler, J.; Cho, S. C.; Adroher, X. C. A Review of Polymer Electrolyte Membrane Fuel Cells: Technology, Applications, and Needs on Fundamental Research. *Appl. Energy* **2011**, *88*, 981−1007.

(11) Bing, Y. H.; Liu, H. S.; Zhang, L.; Ghosh, D.; Zhang, J. J. Nanostructured Pt-Alloy Electrocatalysts for PEM Fuel Cell Oxygen Reduction Reaction. *Chem. Soc. Rev.* **2010**, *39*, 2184−2202.

(12) Alia, S. M.; Jensen, K. O.; Pivovar, B. S.; Yan, Y. Platinum-Coated Palladium Nanotubes as Oxygen Reduction Reaction Electrocatalysts. *ACS Catal.* **2012**, *2*, 858−863.

(13) Zhang, J. L.; Vukmirovic, M. B.; Xu, Y.; Mavrikakis, M.; Adzic, R. R. Controlling the Catalytic Activity of Platinum-Monolayer Electrocatalysts for Oxygen Reduction with Different Substrates. *Angew. Chem., Int. Ed.* **2005**, *44*, 2132−2135.

(14) Wang, J. X.; Inada, H.; Wu, L. J.; Zhu, Y. M.; Choi, Y. M.; Liu, P.; Zhou, W. P.; Adzic, R. R. Oxygen Reduction on Well-Defined Core−Shell Nanocatalysts: Particle Size, Facet, and Pt Shell Thickness Effects. *J. Am. Chem. Soc.* **2009**, *131*, 17298−17302.

(15) Lim, B.; Jiang, M. J.; Tao, J.; Camargo, P. H. C.; Zhu, Y. M.; Xia, Y. N. Shape-Controlled Synthesis of Pd Nanocrystals in Aqueous Solutions. *Adv. Funct. Mater.* **2009**, *19*, 189−200.

(16) Sasaki, K.; Wang, J. X.; Naohara, H.; Marinkovic, N.; More, K.; Inada, H.; Adzic, R. R. Recent Advances in Platinum Monolayer Electrocatalysts for Oxygen Reduction Reaction: Scale-Up Synthesis,

Structure and Activity of Pt Shells on Pd Cores. *Electrochim. Acta* **2010**, *55*, 2645−2652.
(17) Gong, K. P.; Su, D.; Adzic, R. R. Platinum-Monolayer Shell on $AuNi_{0.5}Fe$ Nanoparticle Core Electrocatalyst with High Activity and Stability for the Oxygen Reduction Reaction. *J. Am. Chem. Soc.* **2010**, *132*, 14364−14366.
(18) Kuttiyiel, K. A.; Sasaki, K.; Choi, Y.; Su, D.; Liu, P.; Adzic, R. R. Bimetallic IrNi Core Platinum Monolayer Shell Electrocatalysts for the Oxygen Reduction Reaction. *Energy Environ. Sci.* **2012**, *5*, 5297−5304.
(19) Lim, B.; Wang, J. G.; Camargo, P. H. C.; Jiang, M. J.; Kim, M. J.; Xia, Y. N. Facile Synthesis of Bimetallic Nanoplates Consisting of Pd Cores and Pt Shells through Seeded Epitaxial Growth. *Nano Lett.* **2008**, *8*, 2535−2540.
(20) Zhang, H.; Jin, M.; Wang, J.; Kim, M. J.; Yang, D.; Xia, Y. Nanocrystals Composed of Alternating Shells of Pd and Pt Can Be Obtained by Sequentially Adding Different Precursors. *J. Am. Chem. Soc.* **2011**, *133*, 10422−10425.
(21) Jiang, M.; Lim, B.; Tao, J.; Camargo, P. H. C.; Ma, C.; Zhuc, Y.; Xia, Y. Epitaxial Overgrowth of Platinum on Palladium Nanocrystals. *Nanoscale* **2010**, *2*, 2406−2411.
(22) Long, N. V.; Ohtaki, M.; Nogami, M.; Hien, T. D. Effects of Heat Treatment and Poly(vinylpyrrolidone) (PVP) Polymer on Electrocatalytic Activity of Polyhedral Pt Nanoparticles towards Their Methanol Oxidation. *Colloid Polym. Sci.* **2011**, *289*, 1373−1386.
(23) Gong, K.; Vukmirovic, M. B.; Ma, C.; Zhu, Y.; Adzic, R. R. Synthesis and Catalytic Activity of Pt Monolayer on Pd Tetrahedral Nanocrystals with Co-Adsorption-Induced Removal of Surfactants. *J. Electroanal. Chem.* **2011**, *662*, 213−218.
(24) Lee, Y. W.; Kim, M.; Kim, Z. H.; Han, S. W. One-Step Synthesis of Au@Pd Core−Shell Nanooctahedron. *J. Am. Chem. Soc.* **2009**, *131*, 17036−17037.
(25) Lim, B.; Wang, J. G.; Camargo, P. H. C.; Cobley, C. M.; Kim, M. J.; Xia, Y. N. Twin-Induced Growth of Palladium−Platinum Alloy Nanocrystals. *Angew. Chem., Int. Ed.* **2009**, *48*, 6304−6308.
(26) Yu, X.; Wang, D.; Peng, Q.; Li, Y. High Performance Electrocatalyst: Pt−Cu Hollow Nanocrystals. *Chem. Commun.* **2011**, *47*, 8094−8096.
(27) Xia, Y.; Xiong, Y. J.; Lim, B.; Skrabalak, S. E. Shape-Controlled Synthesis of Metal Nanocrystals: Simple Chemistry Meets Complex Physics? *Angew. Chem., Int. Ed.* **2009**, *48*, 60−103.
(28) Guo, S. J.; Li, J.; Dong, S. J.; Wang, E. K. Three-Dimensional Pt-on-Au Bimetallic Dendritic Nanoparticle: One-Step, High-Yield Synthesis and Its Bifunctional Plasmonic and Catalytic Properties. *J. Phys. Chem. C* **2010**, *114*, 15337−15342.
(29) Ataee-Esfahani, H.; Wang, L.; Yamauchi, Y. Block Copolymer Assisted Synthesis of Bimetallic Colloids with Au Core and Nanodendritic Pt Shell. *Chem. Commun.* **2010**, *46*, 3684−3686.
(30) Wang, L.; Yamauchi, Y. Controlled Aqueous Solution Synthesis of Platinum−Palladium Alloy Nanodendrites with Various Compositions Using Amphiphilic Triblock Copolymers. *Chem.—Asian J.* **2010**, *5*, 2493−2498.
(31) Wang, L.; Nemoto, Y.; Yamauchi, Y. Direct Synthesis of Spatially-Controlled Pt-on-Pd Bimetallic Nanodendrites with Superior Electrocatalytic. *J. Am. Chem. Soc.* **2011**, *133*, 9674−9677.
(32) Crespo-Quesada, M.; Andanson, J. M.; Yarulin, A.; Lim, B.; Xia, Y. N.; Kiwi-Minsker, L. UV-Ozone Cleaning of Supported Poly-(vinylpyrrolidone)-Stabilized Palladium Nanocubes: Effect of Stabilizer Removal on Morphology and Catalytic Behavior. *Langmuir* **2011**, *27*, 7909−7916.
(33) Gasteiger, H. A.; Kocha, S. S.; Sompalli, B.; Wagner, F. T. Activity Benchmarks and Requirements for Pt, Pt-Alloy, and Non-Pt Oxygen Reduction Catalysts for PEMFCs. *Appl. Catal., B* **2005**, *56*, 9−35.
(34) Mayrhofer, K. J. J.; Strmcnik, D.; Blizanac, B. B.; Stamenkovic, V.; Arenz, M.; Markovic, N. M. Measurement of Oxygen Reduction Activities via the Rotating Disc Electrode Method: From Pt Model Surfaces to Carbon-Supported High Surface Area Catalysts. *Electrochim. Acta* **2008**, *53*, 3181−3188.
(35) Alexandridis, P.; Tsianou, M. Block Copolymer-Directed Metal Nanoparticle Morphogenesis and Organization. *Eur. Polym. J.* **2011**, *47*, 569−583.
(36) Piao, Y.; Jang, Y.; Shokouhimehr, M.; Lee, I. S.; Hyeon, T. Facile Aqueous-Phase Synthesis of Uniform Palladium Nanoparticles of Various Shapes and Sizes. *Small* **2007**, *3*, 255−260.
(37) Yang, J. H.; Zhou, W. J.; Cheng, C. H.; Lee, J. Y.; Liu, Z. L. Pt-Decorated PdFe Nanoparticles as Methanol-Tolerant Oxygen Reduction Electrocatalyst. *ACS Appl. Mater. Interfaces* **2010**, *2*, 119−126.
(38) Zhao, Y. C.; Yang, X. L.; Tian, J. N.; Wang, F. Y.; Zhan, L. Methanol Electro-Oxidation on Ni@Pd Core−Shell Nanoparticles Supported on Multi-Walled Carbon Nanotubes in Alkaline Media. *Int. J. Hydrogen Energy* **2010**, *35*, 3249−3257.
(39) Baranova, E. A.; Miles, N.; Mercier, P. H. J.; Le Page, Y.; Patarachao, B. Formic Acid Electro-Oxidation on Carbon Supported Pd_xPt_{1-x} ($0 \geq x \geq 1$) Nanoparticles Synthesized via Modified Polyol Method. *Electrochim. Acta* **2010**, *55*, 8182−8188.
(40) Yang, J. H.; Lee, J. Y.; Zhang, Q. B.; Zhou, W. J.; Liu, Z. L. Carbon-Supported Pseudo-Core−Shell Pd−Pt Nanoparticles for ORR with and without Methanol. *J. Electrochem. Soc.* **2008**, *155*, B776−B781.
(41) Yang, J. H.; Yang, J.; Ying, J. Y. Morphology and Lateral Strain Control of Pt Nanoparticles via Core−Shell Construction Using Alloy AgPd Core toward Oxygen Reduction Reaction. *ACS Nano* **2012**, *6*, 9373−9382.
(42) Shao, M.; Peles, A.; Shoemaker, K. Electrocatalysis on Platinum Nanoparticles: Particle Size Effect on Oxygen Reduction Reaction Activity. *Nano Lett.* **2011**, *11*, 3714−3719.
(43) Sun, S.; Zhang, G.; Geng, D.; Chen, Y.; Li, R.; Cai, M.; Sun, X. A Highly Durable Platinum Nanocatalyst for Proton Exchange Membrane Fuel Cells: Multiarmed Starlike Nanowire Single Crystal. *Angew. Chem., Int. Ed.* **2011**, *50*, 422−426.
(44) Nørskov, J. K.; Rossmeisl, J.; Logadottir, A.; Lindqvist, L.; Kitchin, J. R.; Bligaard, T.; Jónsson, H. Origin of the Overpotential for Oxygen Reduction at a Fuel-Cell Cathode. *J. Phys. Chem. B* **2004**, *108*, 17886−17892.
(45) Stamenkovic, V.; Schmidt, T. J.; Ross, P. N.; Markovic, N. M. Surface Composition Effects in Electrocatalysis: Kinetics of Oxygen Reduction on Well-Defined Pt_3Ni and Pt_3Co Alloy Surfaces. *J. Phys. Chem. B* **2002**, *106*, 11970−11979.
(46) Xu, Z.; Zhang, H.; Zhong, H.; Lu, Q.; Wang, Y.; Su, D. Effect of Particle Size on the Activity and Durability of the Pt/C Electrocatalyst for Proton Exchange Membrane Fuel Cells. *Appl. Catal., B* **2012**, *111−112*, 264−270.
(47) Kim, C.; Oh, J. G.; Kim, Y. T.; Kim, H.; Lee, H. Platinum Dendrites with Controlled Sizes for Oxygen Reduction Reaction. *Electrochem. Commun.* **2010**, *12*, 1596−1599.
(48) Hong, J. W.; Kang, S. W.; Choi, B.-S.; Kim, D.; Lee, S. B.; Han, S. W. Controlled Synthesis of Pd−Pt Alloy Hollow Nanostructures with Enhanced Catalytic Activities for Oxygen Reduction. *ACS Nano* **2012**, *6*, 2410−2419.
(49) Sun, S. H.; Jaouen, F.; Dodelet, J. P. Controlled Growth of Pt Nanowires on Carbon Nanospheres and Their Enhanced Performance as Electrocatalysts in PEM Fuel Cells. *Adv. Mater.* **2008**, *20*, 3900−3904.